Applied Geochemistry 137 (2022) 105207

Contents lists available at ScienceDirect

Applied Geochemistry

journal homepage: www.elsevier.com/locate/apgeochem

A reactive transport modeling perspective on the dynamics of interface-coupled dissolution-precipitation

Hang Deng [a,1,*], Jenna Poonoosamy [b], Sergi Molins [a]

[a] *Lawrence Berkeley National Laboratory, Berkeley, CA, 94720, USA*
[b] *Institute of Energy and Climate Research (IEK-6): Nuclear Waste Management and Reactor Safety, Forschungszentrum Jülich GmbH, 52425, Jülich, Germany*

ARTICLE INFO

Editorial handling by Dr. Z Zimeng Wang

Keywords:
Micro-continuum
Pore-scale reactive transport model
Co-dissolution and precipitation
ICDP
Probabilistic nucleation
Passivation
Coating layer

ABSTRACT

In interface coupled dissolution-precipitation systems, the dynamics of the mineral-fluid interface depends on two intertwining processes: the dissolution of the primary mineral that is needed for subsequent precipitation and the passivation of the dissolution reaction as a result of secondary mineral precipitation. The resulting thickness and texture of the precipitating coating layer will affect the progression of geochemical reactions, flow and transport processes at the macroscopic scale. Understanding the interplay between macroscopic flow regimes and microscopic reaction mechanisms (e.g., nucleation and crystal growth pathways) in controlling the dynamics of the mineral-fluid interface has important implications for predicting natural weathering processes, scaling in the subsurface energy production systems, etc. In this study, we use a micro-continuum pore-scale reactive transport model to investigate the feedback loop between reaction rate and solute transport with explicit consideration of the surface passivation and the diffusion process through the coating layer, as well as the impacts of saturation-dependent nucleation rate on the textures of precipitates that will largely dictate the diffusion properties of the coating layer. Our model results highlight that the drastically different coating behaviors at the macroscopic scale and their dependence on solution supersaturation observed in previous column experiments are primarily controlled by the interplay between mineral reaction rates, advective flow, and diffusion through the dynamically forming coating layer. The diffusion properties of the coating layer also play a secondary but non-negligible role in shaping the evolution of the co-dissolution and precipitation system. The probabilistic nucleation model building on the framework of classical nucleation theory highlights the complex dependence of precipitates' texture on solution chemistry and substrate properties, which can affect the diffusion process within the precipitates. The modeling observations also underscore the necessity of further investigations to better characterize the properties of the coating layer and to improve modeling descriptions of the nucleation processes.

1. Introduction

Interface-coupled dissolution and precipitation (ICDP) reactions are characterized by the dissolution and retreating of the primary mineral surface, coupled with the precipitation of a secondary mineral as a rim (mineral coating) on the surface. The thickness, texture, and tortuosity of the rim control the exchange between the pore fluid and the underlying mineral phases, and thus further mineralogical reactions. ICDP processes play an important role in fluid-rock reactions with implications in various geological and environmental settings (Forjanes et al., 2020; Renard et al., 2019). For instance, carbonate mineralization following the release of cations from mineral dissolution is a key trapping mechanism in geologic carbon storage reservoirs (Metz et al., 2005), and is a crucial process that is involved in many negative emission technologies (Kelemen et al., 2019; National Academies of Sciences, Engineering, and Medicine, 2019) and the degradation of cement and concrete materials (Perko et al., 2020; Qiu, 2020). ICDP reactions may affect the effectiveness of flow pathways (e.g., fractures and pipelines) and thus production in unconventional oil and gas reservoirs (Xiong et al., 2021). Therefore, understanding the factors that regulate the development of the mineral coating (i.e., the rim) is critical for predicting the geochemical reactions and the resulting impacts on various geological and environmental systems over geological time scale.

Reactive transport models can capture the intricate interplay

---

* Corresponding author.
E-mail addresses: hangdeng310@gmail.com, hangdeng@lbl.gov (H. Deng).
[1] Present Address (H.D.) College of Engineering, Peking University, Beijing, China, 100871

https://doi.org/10.1016/j.apgeochem.2022.105207
Received 14 October 2021; Received in revised form 8 January 2022; Accepted 10 January 2022

between reaction kinetics and transport mechanisms including flow and diffusion, thus providing a valuable tool for in-depth examinations and predictions of these systems (Deng et al., 2021a). However, accurate representation of mineral dissolution and crystallization (nucleation and crystal growth) in porous media is still challenging (Deng and Spycher, 2019; Noiriel and Soulaine, 2021; Seigneur et al., 2019; Soulaine et al., 2021). The complexity arises from the dependence of reaction mechanisms on multiple factors, including fluid flow, fluid chemistry and the mineral substrate. Fluid flow controls the mixing of solutes in the pore fluid and can make homogeneous nucleation more favorable than heterogeneous nucleation (Poonoosamy et al., 2020c). The hydrodynamics of the system can also dictate the polymorphism of minerals (Zhang et al., 2010) and crystal morphology (Poonoosamy et al., 2019). Fluid chemistry, in particular the saturation state with respect to the precipitating phase (Poonoosamy et al., 2016), directly influences nucleation mechanisms and reaction kinetics. The mineral substrate can control mineral growth by acting as a crystallographic template for further crystallization of minerals (Nooraiepour et al., 2021b). For example, calcite precipitated preferentially in a porous medium constituted of calcite crystals compared to one composed of aragonite ooids (Noiriel et al., 2012). Mineral precipitation mechanisms have also been shown to depend on the pore size (Rajyaguru et al., 2019).

The description of ICDP in reactive transport models (Varzina et al., 2020) is non-trivial also because the aforementioned factors and complex transport and system dynamics intervene simultaneously. A reactive transport experimental benchmark capturing ICDP was described in (Poonoosamy et al., 2020b) where the effect of fluid chemistry on the dissolution of celestite and epitaxial growth of barite was investigated. The results showed a non-linear relationship between the thickness of the barite rim and the solution saturation with respect to barite. Even in such an advective system, fluid velocity approaches zero at the mineral surface and thus diffusion becomes the dominant mechanism for mass transfer at the mineral-fluid interface and controls the development of precipitation front into the matrix (Deng et al., 2018; Poonoosamy et al., 2020a). Reactants diffuse through the dynamically forming and nano-micro porous coating layer, enabling dissolution and precipitation to continue (Poonoosamy et al., 2020b), but at much slower rates. The other cause for slower reaction rates observed in ICDP systems is the decrease of reactive surface area of the dissolving phase because the coating layer can prevent physical contact with the reactive fluid.

The two main modeling approaches to simulate ICDP are continuum-scale models and pore-scale models. In continuum scale models, the passivation of the subsequent reactions resulting from the rim can be accounted for by using a rate constant that is dependent on diffusion through the rim layer, following the shrinking core model (Mayer et al., 2001). Another treatment for reaction passivation is to constrain the effective reactive surface area by allowing it to decrease with the amount of the remaining dissolving mineral phase while the amount of the precipitating mineral phase increases (Daval et al., 2009; Harrison et al., 2015). These treatments, however, do not explicitly account for the interplay between diffusion and other important chemical-physical processes, and were not able to capture the distinct rim patterns developed under different supersaturations (Poonoosamy et al., 2020b).

Pore-scale reactive transport models can capture the interplay between mineral reactions, flow, diffusion, and pore geometries (Deng et al., 2018; Molins et al., 2021; Molins et al., 2012; Molins et al., 2014; Noiriel and Soulaine et al., 2021), and controlled numerical experiments using pore-scale reactive transport models can isolate individual factors involved in the ICDP systems. This is particularly critical given that direct observation and quantification of diffusion through the coating layer in ICDP is difficult. Pore scale reactive transport modeling has been used to investigate various aspects of mineral crystallization in porous media. Most studies are based on the Lattice Boltzmann method. For instance, (Yoon et al., 2012) modeled mixing induced precipitation of calcite reproducing experimentally observed patterns and rates, and (Chen et al., 2014) compared random crystal growth versus crystallographic direction oriented growth in a diffusive system with co-dissolution and precipitation. The Classical Nucleation Theory (CNT) was also integrated into LBM to examine the effect of pore-size and solution saturation ratio on nucleation mechanisms (Prasianakis et al., 2017) with a probabilistic approach (Fazeli et al., 2020).

Recently, the so-called micro-continuum approach for the simulations of pore-scale reactive transport processes has gained popularity, particularly in systems where mineral precipitation is relevant (Deng et al., 2021b; Yang et al., 2021). The micro-continuum formulation alleviates some challenges of tracking the solid-fluid interfaces resulting from mineral precipitation that are faced by some pore-scale models. (Yang et al., 2021) investigated the impacts of advective flow and diffusion in the pore space, as well as reaction rate on crystal growth of barite. It was observed that the increase in reaction rate and advective transport are more efficient in promoting crystal growth compared to diffusive transport. By implementing reaction rates that depend on crystallographic orientation, the model was able to preserve the shape of the crystal. However, nucleation was not explicitly considered in this work. (Deng et al., 2021b) focused on a diffusive system, while including crystal growth as well as homogeneous nucleation based on the CNT. Their modeling results reproduced precipitation patterns in porous media that have been observed in previous experimental studies (Noiriel et al., 2012; Rajyaguru et al., 2019; Zhang et al., 2010), and offered a tool for numerical experiments on precipitation driven diffusivity change in porous media.

In this study, we build upon recent development in micro-continuum pore-scale reactive transport models that include precipitation dynamics in order to examine the dynamics of ICDP systems. Our objectives are two-fold. First, we evaluate whether the interactions between reaction kinetics and solute transport at the pore scale can explain the dynamics of co-dissolution and precipitation observed experimentally, i.e., the strong dependence of the macroscopic patterns on solution supersaturation (Poonoosamy et al., 2020b). For this purpose, the model was adapted to capture the grain scale process of coating and diffusion, while considering the macroscopic flow and chemistry. Second, we explore how the chemistry of the system – specifically saturation state and substrate properties - can potentially affect nucleation processes, and thus the texture of the precipitates and diffusion through the coating layer. To this end, the model was expanded to combine the classical nucleation theory approach and a probabilistic nucleation module. Section 2 presents the model details and the simulation setup, and Section 3 presents the simulation results and a discussion of the dependence of precipitation patterns and nucleation dynamics on fluid chemistry and kinetic parameters. We conclude our study in Section 4.

2. Methods

In this section, we first present the micro-continuum model (section 2.1) and the mathematical descriptions of the precipitation reaction (sections 2.2-2.3). The model description is then followed by a detailed documentation of the simulation setups for the two modeling tasks corresponding to the dual objectives of our study. The two sets of simulations (section 2.4 and 2.5) both use the micro-continuum model and differ in the mathematical description of the precipitation reaction, using the formulations in section 2.2 and 2.3, respectively.

2.1. Micro-continuum model

In the micro-continuum simulations, the interface between the pore-water and the parent mineral phase can be explicitly tracked, and thus the development of the precipitation layer and diffusion through the coating layer can be explicitly modeled. The micro-continuum model was previously developed for a diffusive system within the reactive transport code CrunchTope (Deng et al., 2021b). For simulations of systems with advective flow, the CrunchTope model was coupled with COMSOL Multiphysics using MATLAB Livelink (v5.6) (Zhang et al., 2022). In the coupled modeling framework, the Darcy-Brinkman equation (eqn (1)) is firstly solved in COMSOL Multiphysics for the velocity field, which is imported into CrunchTope for solving the advection-diffusion-reaction equation (eqn (2)). These two codes are coupled sequentially following the operator splitting approach (Zhang et al., 2022). The coupling time step is relatively coarse following the quasi-steady state assumption, i.e., within the coupling time step, it is assumed that precipitation does not change the flow field significantly. In our simulations, finer time steps on the order of hours were used at the beginning of the simulation, which increased to 50 h after 200 h of simulation time. The precipitation patterns as will be presented later support the selection of the coupling time step.

$$\frac{1}{\varphi}\left(\rho\frac{\partial \boldsymbol{u}}{\partial t}+\rho\boldsymbol{u}\cdot\nabla\left(\frac{\boldsymbol{u}}{\varphi}\right)\right)=-\nabla p+\frac{\mu}{\varphi}\nabla^{2}\boldsymbol{u}-\frac{\mu}{k}\boldsymbol{u} \qquad \text{eqn(1)}$$

where φ (i.e., local porosity) is the volume fraction of the fluid in the grid cell. It is 1.0 in the pore space, 0.0 inside the initial primary mineral phase, and is a fractional value as precipitation progresses and occupies part of the grid cell and as the primary mineral phase dissolves gradually (Fig. 1a). A non-zero minimum porosity can be set such that the secondary mineral does not fill the grid cells completely. This is assuming that the precipitates are porous, which can be a result of the pore-size controlled solubility (PCS) effect and/or local transport limitations (Deng et al., 2021b; Varzina et al., 2020). A value of 10% was used unless specified otherwise. While no direct observations are available for the system that we are modeling, this value is comparable to reported values of residual porosity resulting from the PCS effect for calcium carbonate precipitates (Varzina et al., 2020). $\boldsymbol{u}$ is the pore velocity, p is the pressure, ρ and μ are the density and viscosity of the fluid, respectively. $\boldsymbol{k}$ is the permeability tensor in the medium, and is estimated based on the local porosity using a power law relationship ($k = 0.01\varphi^{5}$). This relationship is somewhat arbitrary as flow in the porous precipitates is not the focus of our study and our goal is to capture the pore flow. Accurate pore flow velocity field can be achieved if the permeability in the pore space and that in the mineral matrix differ by more than four orders of magnitude (Soulaine et al., 2017).

$$\frac{\partial\varphi\Psi_{i}}{\partial t}=-\nabla\cdot(\boldsymbol{u}\varphi\Psi_{i})+\nabla\cdot(\varphi D_{i}\nabla\Psi_{i})-\vartheta_{i}R_{i} \qquad \text{eqn(2)}$$

where Ψ_i is the total concentration of a chemical component, D_i is the diffusion coefficient, which is equal to the molecular diffusion coefficient (D_m) in the pore space, and is $D_m\varphi^m$ in grid cells occupied by the precipitates to account for the tortuosity caused by the presence of the solid phase. The exponent m was set to be 2 unless specified otherwise. The last term on the right-hand side is the reaction term that accounts for the concentration change caused by mineral reactions, with ϑ_i being the stoichiometric coefficient.

2.2. Mineral growth

Mineral precipitation and dissolution can both be described by the transition state theory rate law,

$$R_{i}=Ak_{rxn}\left(1-\frac{IAP}{K_{sp}}\right) \qquad \text{eqn(3)}$$

where k_{rxn} $[mol/m^2 s]$ is the rate constant, IAP is the ionic activity product, and K_{sp} is the solubility. The solubilities for celestite and barite are $10^{-6.63}$ and $10^{-9.97}$ at 25 C, respectively, as used in the experimental study of (Poonoosamy et al., 2020b). In the micro-continuum approach, the surface area (A $[m^2/m^3]$) is calculated from the spatial gradient of porosity (φ) (eqn (4)) (Deng et al., 2021b; Luo et al., 2012; Soulaine et al., 2017), and the reactive surface area of a given mineral (A_i) is weighted by the five point average of the volumetric fraction of the corresponding mineral ($\overline{f_{v_i}}$) (Fig. 1b) (eqn (5)). As such, the coating of the parent mineral phase and thus the passivation of its dissolution is explicitly accounted for.

$$A=\nabla\varphi \qquad \text{eqn(4)}$$

$$A_{i}=A\cdot\overline{f_{v_i}} \qquad \text{eqn(5)}$$

2.3. Probabilistic nucleation

Classical nucleation theory (eqn (6)) rather than the transition state theory rate law may be used to describe the precipitation process. For the celestite-barite mineral system investigated, the precipitation process involves the heterogeneous nucleation of barite on celestite and on barite. Homogeneous nucleation is not considered because of the much higher energetic barrier. The heterogeneous nucleation rate [mol/m^2 substrate s] is calculated from the following equations (Prieto, 2014):

$$J=\Gamma exp\left(-\frac{\Delta G_{c}}{kT}\right) \qquad \text{eqn(6)}$$

where k is the Boltzmann constant, T is the temperature [K]. The Gibbs free energy term is given as follows:

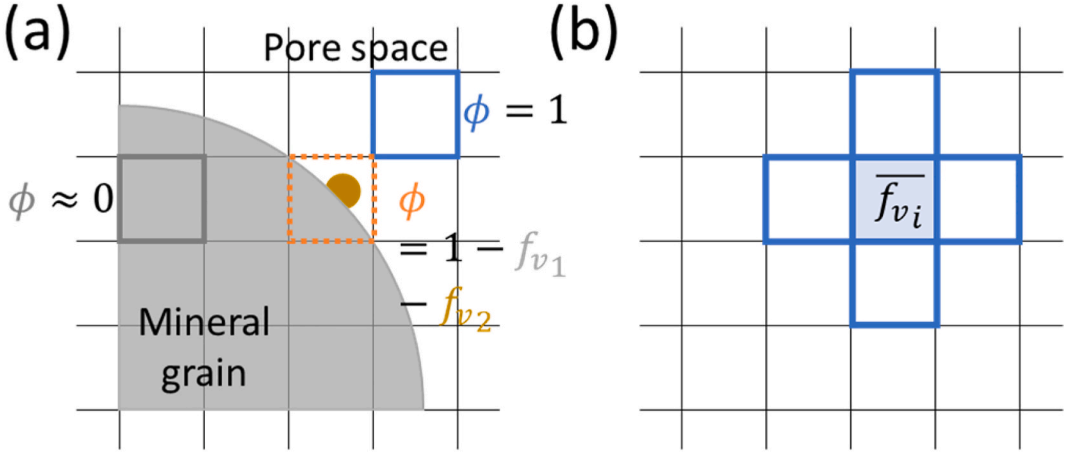

Fig. 1. (a) Conceptual illustration of the micro-continuum approach, in which a local porosity field (φ) is used to represent the mineral grain (gray solid), the pore space, and the interface where precipitation (brown solid) occurs; and (b) illustration of the five-point weighting scheme, the cell for which the mineral specific area is calculated is highlighted in light blue, and the thick blue lines outline the five grid cells, the mineral fractions of which are used in the calculation of eqn (5). (For interpretation of the references to colour in this figure legend, the reader is referred to the Web version of this article.)

$$\Delta G_c = \frac{16\pi v_0{}^2 \gamma^3}{3(kTln\Omega)^2} \qquad \text{eqn(7)}$$

where v_0 is the molecular volume, γ is the effective surface tension, and $\Omega = \frac{IAP}{K_{sp}}$ is the supersaturation.

The pre-exponential term (Γ) is a function of the nucleation sites density (N_0, [# nuclei/m^{2}substrate]), the number of monomers per unit volume of fluid (N_1, [# monomers/m^3 fluid]), and the diffusion coefficient of the monomer (D). N_0 is approximated by dividing the unit surface area by the cross-section area of the critical nuclei, and N_1 can be readily calculated from the local concentration of the monomer. Z in the equation is a function of the Gibbs free energy and the number of the critical nuclei (n_c). The radius of the critical nuclei (r_c) is given by eqn (11).

$$\Gamma = 4\pi Z D N_0 N_1 r_c \qquad \text{eqn(8)}$$

$$Z = \sqrt{\left(\frac{\Delta G_c}{3\pi kT(n_c)^2}\right)} \qquad \text{eqn(9)}$$

$$n_c = \left(\frac{2\sigma a}{3kTln\Omega}\right)^3 \qquad \text{eqn(10)}$$

$$r_c = \frac{2\sigma v_0}{kTln\Omega} \qquad \text{eqn(11)}$$

In conjunction with the CNT, a probabilistic approach is included. Similar to (Fazeli et al., 2020; Nooraiepour et al., 2021a), a random variable that follows a normal distribution ($x \in N(0,\ 1)$) is used to introduce a stochastic induction time (τ_p) based on the induction time given by the theoretical calculation following the CNT (τ_N)

$$\tau_p = \frac{x + n\sigma}{n\sigma} \cdot \tau_N \qquad \text{eqn(12)}$$

where σ is the standard deviation of the normal distribution and equals to 1 in our case, and $n = 4$, capturing 99.9% of the population in the normal distribution. As a result, the probabilistic induction time falls in $(0,\ 2\tau_N]$. Instead of using the induction time to update the surface area of the nuclei and a deterministic crystal growth rate as in (Fazeli et al., 2020), our model simulates the precipitation rate as heterogeneous nucleation of the barite on both celestite and barite, and the nucleation rates are calculated from the CNT rate laws (eqn(6-11)) and adjusted according to the probabilistic induction time.

$$J_p = J \cdot \frac{\tau_N}{\tau_p} \qquad \text{eqn(13)}$$

Thus, in the probabilistic modeling of the precipitation reaction, the reaction rate is given by

$$R_i = \sum_j A_j \cdot J_{p,j} \qquad \text{eqn(14)}$$

where subscript j denotes the substrate for the nucleation of barite.

2.4. Streamline simulations

These simulations were designed to investigate the evolution of distinct coating patterns along the flow direction under different supersaturation conditions as reported in (Poonoosamy et al., 2020b), and thus they follow the chemical and flow conditions of the column experiments. In the experiments, celestite grains with size of ~50 μm were packed in a 1.1 cm long column with a porosity of 46 ± 2%. Influents of different $BaCl_2$ concentrations (1 mM, 10 mM, and 100 mM) were injected at the same flow rate of 2.5×10^{-10} m^3/s through the column, resulting in celestite dissolution and barite precipitation on the remaining celestite grains. Rather than a direct simulation of the spatial complexity of the experimental system, we focus on the simulation of precipitation along a flow path that follows the tortuous pore space existing between the celestite grains as supersaturation conditions evolve. The geometry used in our simulations (Fig. 2 a&b) is equivalent to following a streamline (Poonoosamy et al., 2020a).

Based on the grain size and porosity of the celestite column used in the experiment, the width of the domain was set to 50 μm. Half of the domain was initially occupied by the celestite mineral phase and the other half by DI water. The computational domain was 5 cm long, which is equivalent of assuming a tortuosity factor of approximately five for the celestite column. The tortuosity factor measures the ratio between the length of the streamline and the length of the column, and is usually inferred from effective diffusivity. The value used here is based on the diffusivity measurements for packed quartz sand columns with similar porosities in prior experiments (Chagneau et al., 2015), and thus provides a reasonable approximation. The flow and reactive transport are described by eqns (1) and (2) and celestite dissolution and barite precipitation are both described by eqn (3). The kinetic coefficients (k_{rxn}) have values of $10^{-5.66}$ mol/m^{2}s for celestite (Marty et al., 2015), and $10^{-7.9}$ mol/m^{2}s for barite (Palandri, 2004).

2.5. Probabilistic nucleation simulations

In order to investigate the impacts of local chemical conditions on nucleation processes near the mineral surface - and thus the texture of the precipitates - we used a shorter section of the streamline domain (Fig. 2c), which allows for a resolution of 0.5 μm using a 100 × 100 grid. The domain is divided into two halves, occupied by celestite and DI water initially, respectively. It is similar to what is illustrated in Fig. 2b, but with different dimensions and resolution. For simplicity, advective flow was not considered in the nucleation simulations. Celestite dissolution was modeled by the same kinetic treatment as described in section 2.4., i.e., using eqn (3). Barite precipitation, however, is described with eqns(6-14). The effective surface tension (γ) is 45 mJ/m^2 for the celestite-barite interface (Poonoosamy et al., 2016), and 22.8 mJ/m^2 for the barite-barite interface (Ruiz-Agudo et al., 2015). D is 0.963×10^{-9} m^2/s, and N_0 is ~4.2453×10^{18} nuclei/m^{2}substrate. Since it uses a finer resolution with very small grid cells, precipitation within each grid cell is allowed to progress unless local porosity approaches zero. In the process, the diffusivity is corrected by the local porosity (i.e., $D_m\varphi$).

The left boundary is connected to a $BaCl_2$ solution, and the right boundary is in contact with DI water. Three subsets of simulations were performed to investigate the impacts of the saturation state and the properties of the substrate. $BaCl_2$ concentrations of 10 mM and 100 mM were compared, and an additional subset was simulated with the high $BaCl_2$ concentration but lowering the nucleation site density on celestite (N_0) by 1000 times. For each simulation scenario, 30 realizations were conducted.

Table 1 compares the setup of the streamline and the probabilistic nucleation simulations to highlight the major differences.

3. Results & discussion

3.1. Dependence of coating patterns on solution supersaturation

Overall, the simulations captured the major observations from the experimental study of (Poonoosamy et al., 2020b). Figs. 3–5 show the effluent chemistry in comparison with the experimental measurements and barite coating patterns from the simulations with three different solution supersaturations.

In the simulation with the highest $BaCl_2$ concentration of 100 mM (Fig. 3), uniform barite coating was observed throughout the celestite column. The thickness of the coating layer was estimated by counting the number of grid cells in which barite was observed (i.e., with a volume fraction ≥ 10%). By the end of the simulation, which is 500 h as in the experiments, the thickness reaches ~5 μm. It is comparable to the

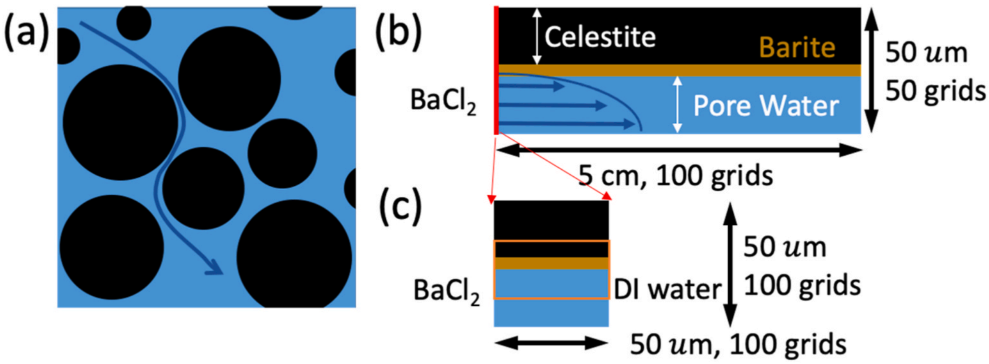

Fig. 2. (a) illustration of a streamline in a porous media; (b) the computational domain that follows the streamline; (c) computational domain for the probabilistic nucleation simulations, and the orange box highlight the region shown in Figs. 7–9. (For interpretation of the references to colour in this figure legend, the reader is referred to the Web version of this article.)

Table 1
Summary of the setup of the streamline simulations and the probabilistic nucleation simulations (L-left, R-right, B-bottom, T-top).

	Streamline simulations	Probabilistic nucleation simulations
Focuses	Macroscopic precipitation patterns and the dependence on supersaturation state	Precipitates' texture and the dependence on supersaturation state and substrate properties
Domain illustration	Fig. 2a and b	Fig. 2c
Flow boundary conditions	L - constant average velocity R- constant pressure B - symmetry T – no-slip wall	N/A
Flow initial conditions	Zero	N/A
Reactive transport boundary conditions	L - constant BaCl$_2$ concentration R - DI water B – constant gradient of zero T – constant gradient of zero	L - constant BaCl$_2$ concentration R - DI water B – constant gradient of zero T – constant gradient of zero
Reactive transport initial conditions	Top domain – celestite + DI water Bottom domain – pore space + DI water	Top domain – celestite + DI water Bottom domain – pore space + DI water
Celestite dissolution	TST, i.e., Eqn (3)	TST, i.e., Eqn (3)
Barite precipitation	TST, i.e., Eqn (3)	Probabilistic heterogeneous nucleation, i.e., Eqn(6)-(14)
Minimum porosity in the precipitates	5–10%	Effectively zero

experimental data quantified from the SEM images, which is 2.9 ± 0.8 μm (Table 2). The variations in the experimental data reflect local heterogeneity in the pore structures. As the coating layer develops, the effluent Ba concentration increases while Sr concentration decreases substantially. By hour 500, the Ba concentration reaches ~98 mM and Sr concentration drops to 1.6 mM. This indicates an increasing passivation of celestite dissolution as also clearly shown in the experimental effluent chemistry. In the experiment, a non-zero concentration for Sr was reported towards the end of the experiment, varying between 1.7 and 3.3 mM for the last 100 h, which confirms the existence of the diffusive flux through the coating layer and that the model setup captured the diffusive flux well.

In the simulation, the effluent chemistry shows four distinct stages: a sharp change at the beginning up to ~80 h, a quasi-steady state until hour ~300, a steady state for the last ~150 h, and a transition between the two steady states. In the first stage, the celestite surface is partially covered, and the coverage and thus passivation effect continues to increase as the reactions progress (Fig. 3c hour 20 and 80). This stage ends when a base layer of barite precipitates with minimum porosity is formed (Fig. 3c hour 80). Afterwards, subsequent precipitation occurs on the base layer of barite. In this stage, the new precipitates have not reached the minimum porosity and thus the diffusion constraint is dictated by the more compact base layer (e.g., Fig. 3c hour 200). As such, the continuous reaction does not affect effluent chemistry. The next steady state stage is reached when the base layer with the minimum porosity thickens (e.g., Fig. 3c hour 500). Thus, this behavior is a result of the model setup regarding the development of the coating layer and is sensitive to the porosity-diffusivity relationship as well, and is further discussed below.

At the intermediate BaCl$_2$ concentration of 10 mM (Fig. 4), the Barite coating layer was predicted both in the upstream and the middle sections, as observed in the experiment. In the simulation, the thickness is 5 μm at the inlet, and increases along the flow direction and reaches a maximum of 10 μm half way through the computational domain. The thickness decreases until no coating is present in the downstream section. The experimental data also reported a thicker coating layer in the middle section (4.8 ± 1.3 μm, Table 2) than in the upstream (2.4 ± 1.5 μm, Table 2) (Poonoosamy et al., 2020b). About 25% of the celestite surface in the computation domain close to the outlet is not covered by barite precipitates, and thus celestite dissolution is sustained. Accordingly, the effluent Sr concentration stays at 10 mM throughout the simulation. The effluent is depleted of Ba as it is completely consumed by the precipitation reaction. The effluent chemistry also reproduced concentrations measured in the experiment.

The simulation for BaCl$_2$ concentration of 1 mM predicted similar trends in the effluent chemistry, i.e., constant Sr concentration of ~1.33 mM and Ba concentration of effectively zero (Fig. 5). The Sr concentration is proportional to the influent Ba concentration because consumption of sulfate by barite precipitation is the key thermodynamic driving force for continuous celestite dissolution and the stoichiometric ratio between Sr and sulfate is one. With the lowest influent Ba concentration, the barite coating layer was only observed in the first several millimeters of the computational domain due to fast depletion of Ba in the solution. The experimental Sr concentration is slightly lower than the modeling results because under this experimental condition the precipitating phase is a solid solution that includes Sr, rather than a pure barite phase as considered in the model. The simulation results agree very well with the experiment, which showed highly localized barite precipitation in the first ~500 μm close to the inlet of the column (Table 2). The thickness estimate from the simulation peaks at ~25 μm, which is comparable to celestite grain size. Significant celestite dissolution at the inlet was also observed in the simulations, which is consistent with the experimental observation from the SEM image that a number of celestite grains were completely replaced by barite (Poonoosamy et al., 2020b). The maximum thickness of the coating layer

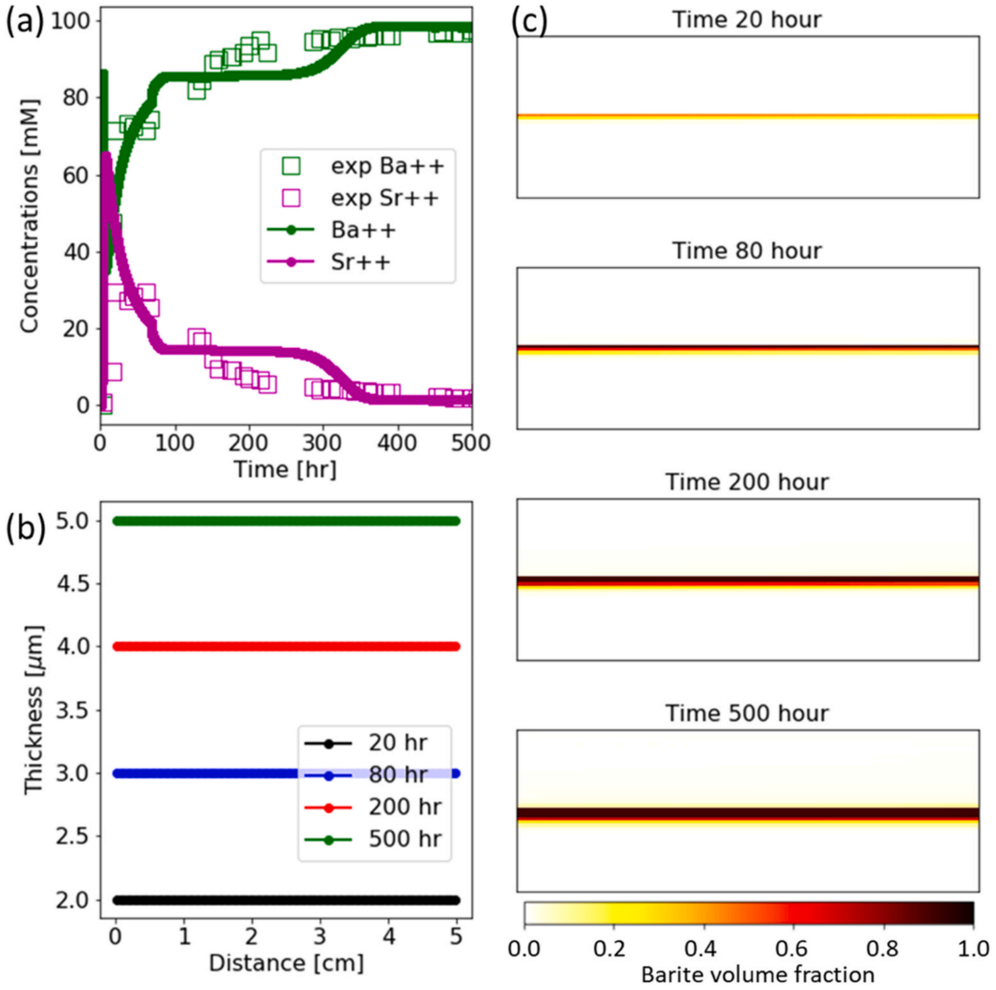

Fig. 3. Results of the simulation with an influent $BaCl_2$ concentration of 100 mM. (a) effluent concentration of Ba^{2+} (green) and Sr^{2+} (magenta) in comparison with the experimental measurements (hollow squares); (b) thickness of the precipitating barite layer, which is calculated by counting the number of grid cells in which barite accounts for more than 10% of the volume; and (c) maps of barite volume fraction in the computational domain at hour 20, 80, 200, and 500. (For interpretation of the references to colour in this figure legend, the reader is referred to the Web version of this article.)

based on the SEM images reaches 16.3 μm (Table 2).

In the experiment, the total amount of barite as estimated from the effluent chemistry at the end is 4.5, 4.36 and 0.45 mmol for the 100, 10, and 1 mM influent solutions, respectively (Poonoosamy et al., 2020b). The model predicted very similar trends among the three simulations. The barite volume is 2.02, 1.62, and 0.162 mm^3, assuming that the 2D cross section has a thickness of 1 mm.

Compared to the continuum-scale reactive transport model performed on the same experimental system in (Poonoosamy et al., 2020b), which accounted for the passivation effect by using a surface area model that relies on empirical and fitted parameters, our model explicitly accounted for surface passivation and the slow-down of the reaction process due to diffusion using parameters with specific physical meanings. As a result, we reproduced precipitation patterns that the continuum-scale model failed to capture using the same kinetic coefficients. Specifically, the thicker coating in the middle section observed in the intermediate Ba^{2+} concentration experiment and the sharp precipitation and dissolution front in the low Ba^{2+} concentration experiment.

In summary, in spite of the conceptual simplifications included in the simulations, we observed good agreement between the simulation results and the experimental observations regarding both fluid chemistry and coating patterns. This highlights that the dependence of the co-dissolution and precipitation dynamics on the solution supersaturation observed in the experiment is primarily controlled by the interplay between macroscopic flow, diffusion through the coating layer and mineral reaction kinetics. Some discrepancy was noted between the experiments and the simulations. For instance, under the intermediate $BaCl_2$ concentration condition, the coating layer thickness from the simulation is about twice of the value that was reported in the experiment.

3.2. *Sensitivity analyses*

Additional simulations were performed to evaluate how the model assumptions, especially regarding the diffusion process through the precipitates, affect the development of the coating layer. The modeling results using two different porosity-permeability relationships, i.e., $k = 10^{-5}\varphi^5$ and $k = 10^{-5}\varphi^3$, are very similar to the results presented above and thus are not discussed further (Figs. S1 and S2). In contrast, noticeable differences are observed in simulations with varied diffusion constraint. Two cases are discussed here.

In one case, the minimum porosity was reduced from 10% to 5% while the local diffusivity-porosity relationship was kept the same. This means that local diffusivity limitation can be stronger. In previous simulations, the minimum local diffusivity is 0.01 D_m, and it is 0.0025 D_m here. The overall behavior of the three simulations of different solution chemistries (Fig. 6) are similar to what were shown above and in the previous experimental study. However, the thickness of the coating layer is consistently smaller. By hour 500, the coating layer is 4 μm thick in the simulation with the highest influent $BaCl_2$ concentration. The stronger diffusion constraint also results in a sharper and more significant change in the effluent concentrations at the early stage, and lower Sr steady state concentrations, e.g., ~0.64 mM at hour 500, compared to ~1.6 mM in the simulation above. For the intermediate influent concentration simulation, the modification in the input parameters results

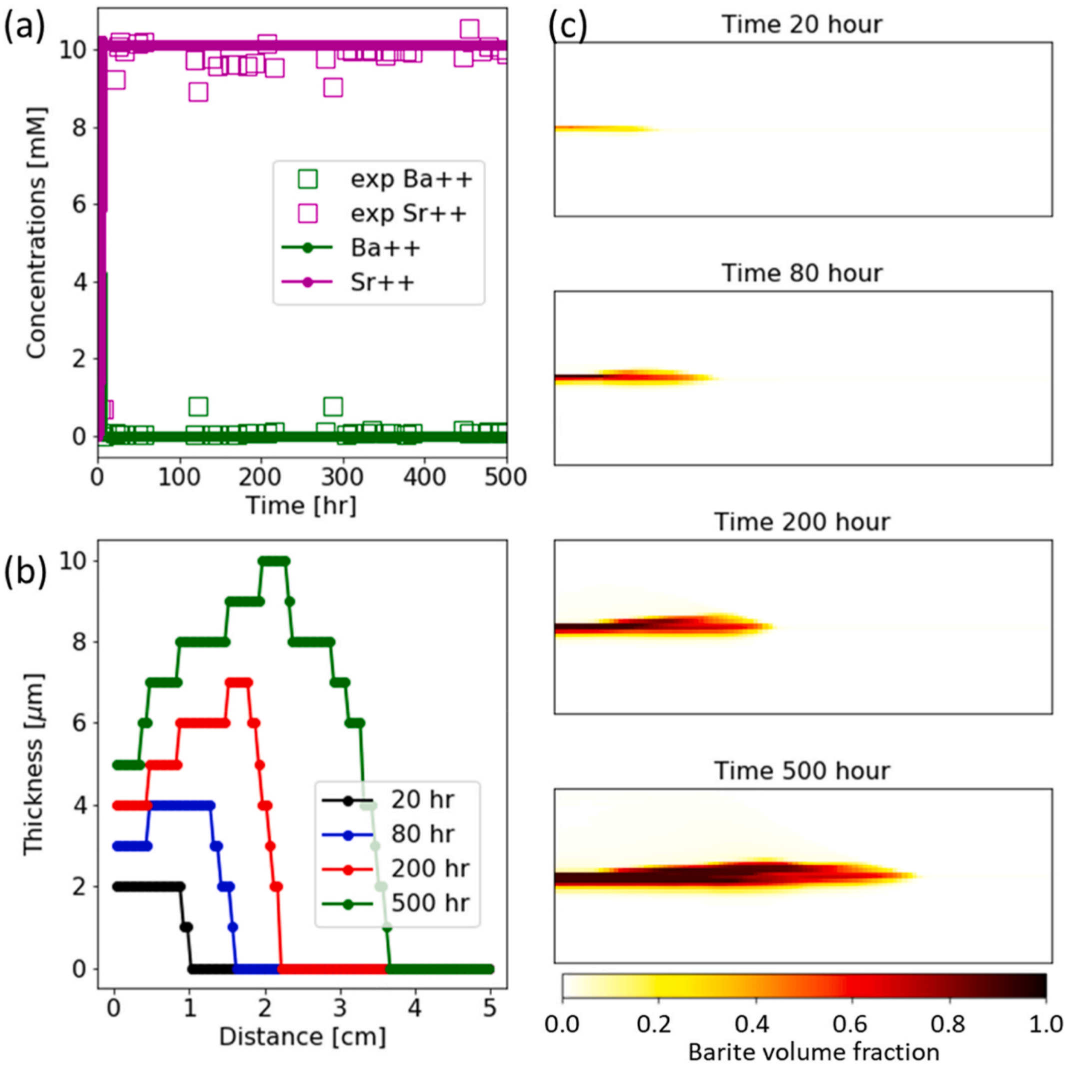

Fig. 4. Results of the simulation with an influent $BaCl_2$ concentration of 10 mM. (a) effluent concentration of Ba^{2+} (green) and Sr^{2+} (magenta) in comparison with the experimental measurements (hollow squares); (b) thickness of the precipitating barite layer, which is calculated by counting the number of grid cells in which barite accounts for more than 10% of the volume; and (c) maps of barite volume fraction in the computational domain at hour 20, 80, 200, and 500. (For interpretation of the references to colour in this figure legend, the reader is referred to the Web version of this article.)

in a coating layer thickness of 4 μm and 6 μm at the inlet and in the middle section, respectively. In addition, the coating layer started to develop in the downstream regions as the stronger diffusion constraint limited transverse transport of Ba^{2+} and barite precipitation at the upstream, and more Ba^{2+} is transported to the downstream and becomes available for precipitation close to the outlet. Towards the end of the simulation, the entire celestite surface becomes coated by barite. As a result, the passivation effect manifests in effluent chemistry, i.e., the Sr concentration starts to decrease and Ba concentration starts to increase.

In the other case, the diffusion constraint was relaxed by reducing the exponent used in the porosity-diffusivity relationship from 2 to 1.5 while keeping the same minimum porosity. As a result, the minimum local diffusivity is increased by a factor of 3. Similar to changing the minimum porosity, the distinct patterns across the three solution chemistries are preserved, and the major difference between this subset of simulations and the ones reported in Figs. 3–5 is the consistently thicker coating layer (Fig. S3). The maximum thickness reaches 7 μm in the high supersaturation simulation and at the inlet of the intermediate supersaturation simulation. As indicated by the barite volume fraction maps, the increase in the thickness - measured by counting the grid cells with ≥10% occupied by barite - is not because the compact barite layer has thickened. Rather, it is because more barite precipitation has developed in the celestite matrix as celestite dissolves and creating local porosity, which has higher local diffusivity due to the modified porosity-diffusivity relationship.

Simulations were also performed with grid cell sizes that are 0.5 and 2.5 times of the default grid cell size. As shown in Figs. S4 and S5, the overall precipitation patterns are consistent with the reference simulations (Figs. 3–5), but some quantitative differences are observed in the thickness of the precipitation layer. A higher resolution results in a thinner coating layer, with the maximum value being 5, 7.5 and 19.5 μm, respectively, for the high, intermediate and low $BaCl_2$ concentration case. The lower resolution simulations show larger thickness, and the maximum values are 7.5, 12.5 and 25 μm for the three cases. The differences are partly a result of how thickness is measured in the simulations as explained above, but mostly reflect the changes in the extent of the precipitation reaction. Our observations are consistent with previous studies that showed faster clogging (i.e., a smaller amount of precipitate) in finer meshes (Liu and Jacques, 2017; Marty et al., 2009). This is because the smaller grid size helps maintain a sharper concentration gradient and thus a sharper reaction front. This is also because the formulation of diffusivity is sensitive to the mesh size. With the same amount of precipitate, a smaller (larger) grid cell would have a smaller (larger) porosity and thus diffusivity. Therefore, reducing the mesh size

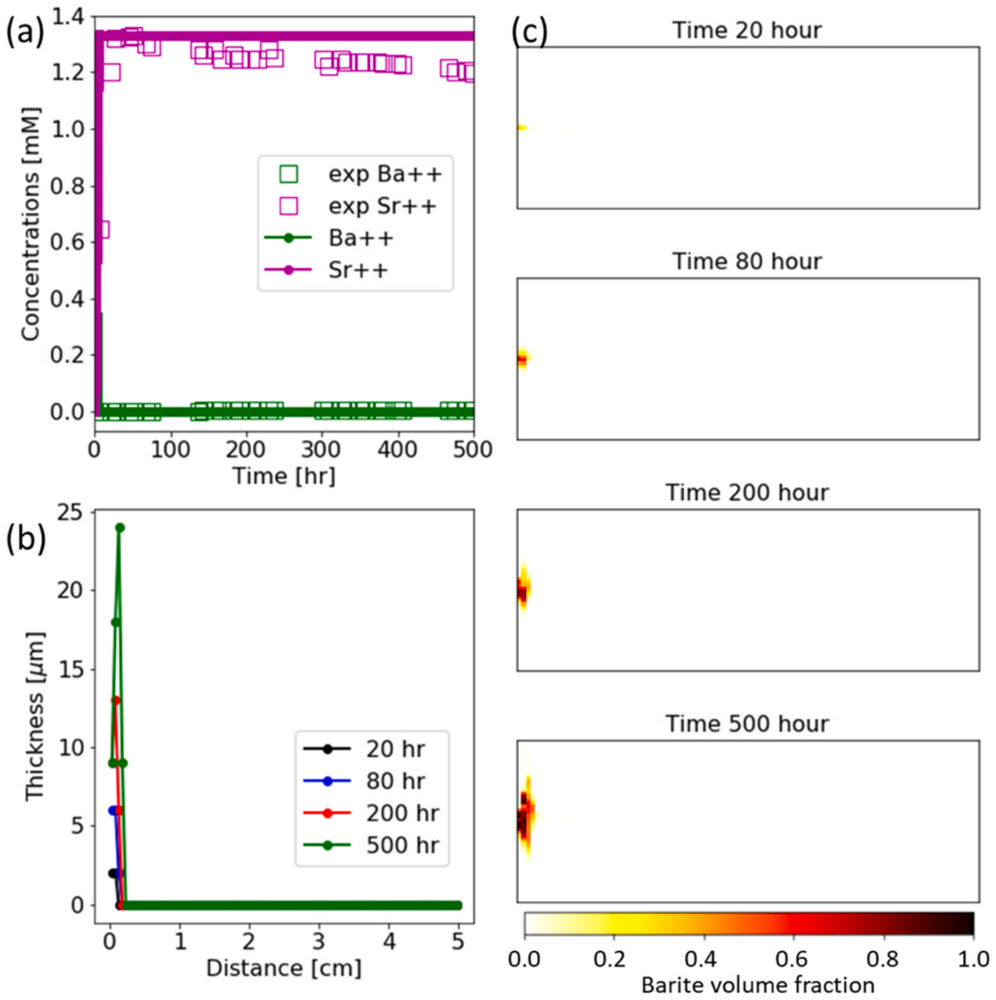

Fig. 5. Results of the simulation with an influent $BaCl_2$ concentration of 1 mM. (a) effluent concentration of Ba^{2+} (green) and Sr^{2+} (magenta) in comparison with the experimental measurements (hollow squares); (b) thickness of the precipitating barite layer, which is calculated by counting the number of grid cells in which barite accounts for more than 10% of the volume; and (c) maps of barite volume fraction in the computational domain at hour 20, 80, 200, and 500. (For interpretation of the references to colour in this figure legend, the reader is referred to the Web version of this article.)

Table 2
Thickness of the coating layer from the (Poonoosamy et al., 2020b) experiments, estimated from SEM (Scanning Electron Microscope) imaging. Location: 0 mm – inlet, 11 mm – outlet. N – number of data points.

Experiment	Location (mm)	Coating layer thickness (μm)			
		min	max	mean	std (N)
1	0–11	1.334	4.7	2.9	0.8 (15)
2	0–3.5	1.149	4.598	2.4	1.5 (5)
	3.5–9.5	2.873	6.897	4.8	1.3 (7)
	9.5–11			0	
3	0–0.5	33.881	16.31	7.4	3.6 (11)
	0.5–11			0	

has the same effect of increasing the diffusive constraint, and vice versa.

3.3. *Dependence of precipitates texture on fluid chemistry and substrate properties*

The sensitivity simulations above further support that the primary controlling factor for the experimentally observed dependence on solution supersaturation of the co-dissolution and precipitation dynamics is the interplay between flow, diffusion and reaction kinetics. However, the secondary effect of the texture and thus diffusion properties of the precipitating layer, which are influenced by complex precipitation mechanisms, can have a non-negligible effect on the system evolution. The sensitivity analyses explored the two key parameters used to describe the diffusion process across the coating layer in the model: the minimum porosity and the exponent used in the porosity-diffusivity relationship. The minimum porosity, also known as residual porosity, is dependent on pore-size controlled solubility and/or local transport limitations, as discussed in (Deng et al., 2021b; Varzina et al., 2020). The evolution of local tortuosity and thus diffusivity in relation to porosity within the precipitates is also quite uncertain. While the most basic porosity-diffusivity relationship and the most common exponent were used in the simulations and showed reasonably good results, variations in the relationship or the exponent could introduce noticeable variations in the coating layer development. Characterization of the coating layer using tools such FIB-SEM can provide critical information for evaluating the porosity of the precipitates or for inferring diffusivity. In absence of such data, the probabilistic nucleation simulations described in Sec. 2.5 are used here to initiate investigations that can provide some insights regarding the textures and thus transport properties of the precipitates. Because we do not make any assumptions of subgrid pore sizes, we cannot account for the PCS effect, and the texture within the precipitates will be primarily controlled by local transport, in addition to the nucleation rate which has a complex dependence on supersaturation and substrate properties.

Fig. 7 shows 30 realizations of the probabilistic nucleation simulations with a $BaCl_2$ concentration of 10 mM (Section 2.5). After 5 h, there is limited amount of precipitation. Overall, the barite precipitates coat the interface relatively uniformly, except for a few cases in which big cluster(s) developed on the interface. In contrast, the simulations with a $BaCl_2$ concentration of 100 mM showed more precipitation after 5 h as expected. The patterns of the precipitates are also distinct from the lower $BaCl_2$ concentration simulations (Fig. 8). More realizations show

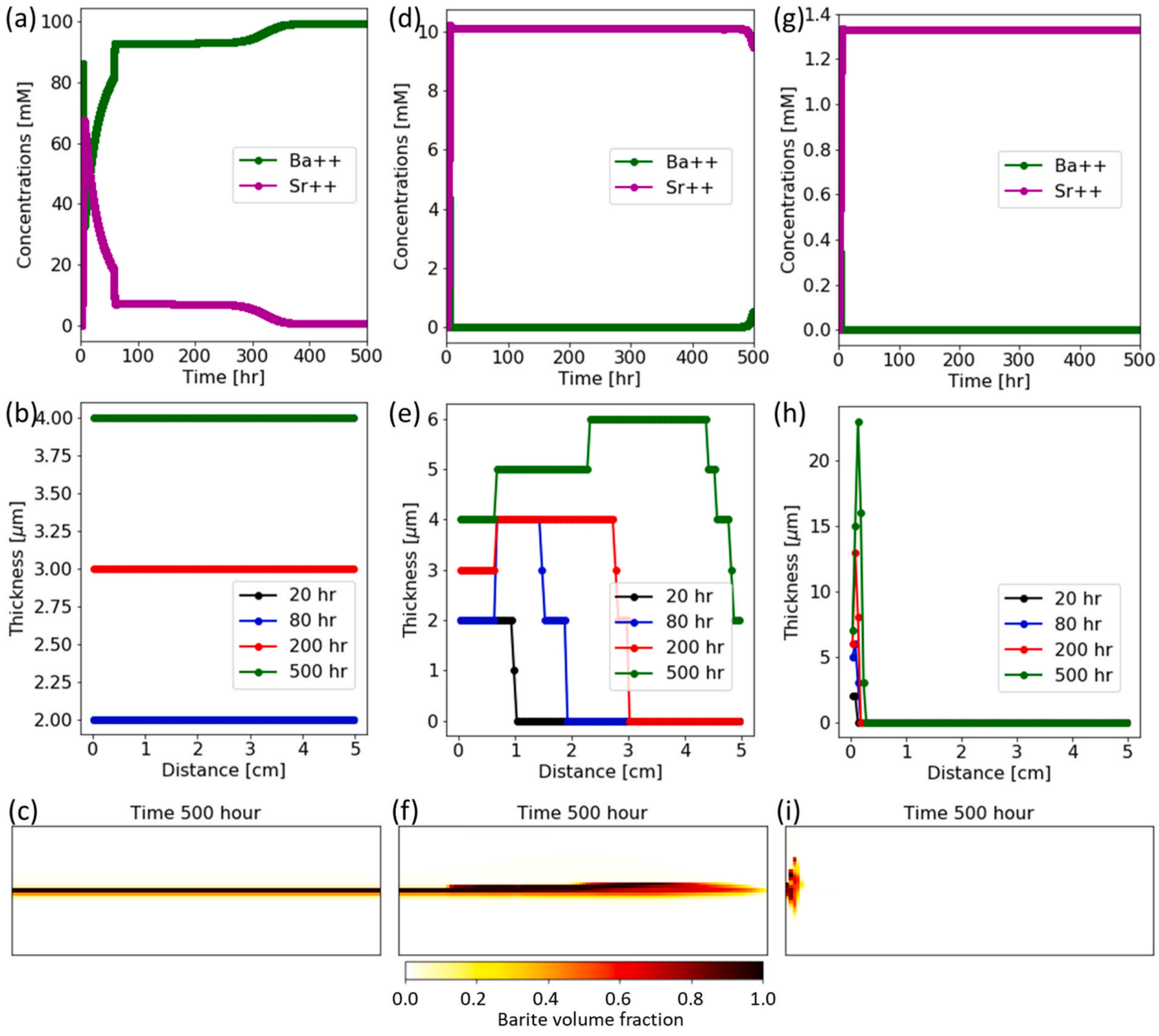

Fig. 6. Simulation results with a minimum porosity of 5% for an influent $BaCl_2$ concentration of (a–c) 100 mM, (d–f) 10 mM, and (g-I) 1 mM. (a) (d) (g) Effluent concentration of Ba^{2+} (green) and Sr^{2+} (magenta). (b) (e) (h) Thickness of the precipitating barite layer, which is calculated by counting the number of grid cells in which barite accounts for more than 10% of the volume. (c) (f) (i) maps of barite volume fraction in the computational domain at hour 500. (For interpretation of the references to colour in this figure legend, the reader is referred to the Web version of this article.)

clusters of precipitates rather than well distributed precipitation. We note that this observation is different from that of (Fazeli et al., 2020), which showed more uniform precipitation at the higher supersaturation. This is because in our model, crystal growth is modeled as heterogeneous nucleation on the mineral itself with a probabilistic rate that has a more complex dependence on local supersaturation state (eqns(6-11)), whereas in the study of (Fazeli et al., 2020), the crystal growth is modeled by a deterministic kinetic coefficient and a linear dependence on the supersaturation state.

To further account for the potential effect of the substrate properties, a subset of simulations was performed with the high $BaCl_2$ concentration but using a site density (N_0) on celestite that is 1000 time lower than that on barite. As a result, the kinetics of nucleation on celestite is even slower than nucleation on barite compared to the setup when effective surface tension (γ) is the only parameter used to prescribe the different energetic barriers based on substrate. In this subset of simulations, the texture of the precipitates is more distributed (Fig. 9) compared to the simulations for which the same site density was used for celestite and barite. None of the realizations predicted the formation of big clusters of precipitates.

To evaluate the potential impacts of the distinct textures on the diffusion process across the coating layer and thus the co-dissolution and precipitation dynamics, the total amount of the precipitates, the porosity within the precipitates and surface coverage were quantified for all the simulations and plotted in Fig. 10. Barite volume was calculated assuming a thickness of 1 mm for the 2D domain. The precipitate porosity was calculated as a ratio between the total amount of barite and the total volume of grid cells with >10% occupied by barite. It should be noted that the porosity measurement defined here is meant for comparison across simulations, and would vary based on the threshold value used to determine the total volume of grid cells occupied by barite in the calculation. The surface coverage was evaluated using the average of barite volume fraction at the interface. A larger surface coverage indicates a stronger passivation effect, whereas a larger porosity is likely to have weaker transport limitation and thus a larger diffusive flux. The amount of barite precipitates is significantly lower for the 10 mM $BaCl_2$ concentration simulations. The surface coverage is lower in this case, whereas the porosity of the precipitates is larger compared to the other two tests with the higher $BaCl_2$ concentration. Between the two cases with higher $BaCl_2$ concentration, the simulations with lower site density on celestite result in slightly more barite precipitation, comparable porosity in the precipitates, but noticeably higher surface coverage.

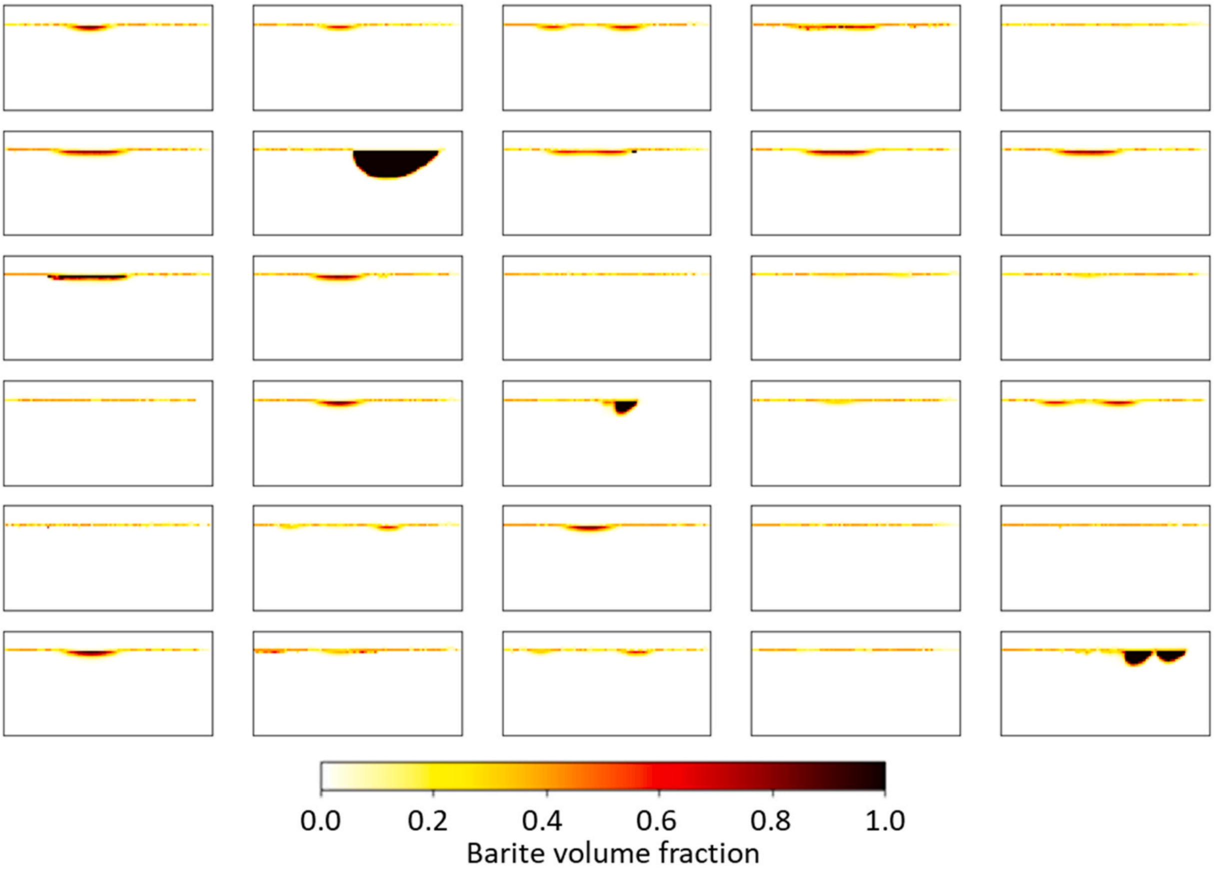

Fig. 7. Maps of the barite precipitation from 30 realizations of the probabilistic nucleation simulations with a $BaCl_2$ concentration of 10 mM and the same nucleation density on both celestite and barite. The domain is trimmed to focus on the interface.

The larger barite volume and surface coverage for the case with lower site density on celestite may appear to be counter-intuitive. In this case, as nucleation on celestite becomes much slower, more reactants are consumed by faster nucleation on barite. This would also trigger positive feedback with surface area, as more barite surface being created, more nucleation on barite is expected. The higher surface coverage is also a result of our conceptualization of the nucleation process, which doesn't consider the crystalline orientation. This means that nucleation perpendicular to and parallel to the interface is not differentiated. As such, a grid cell on the celestite surface that also neighbors a grid cell of barite can have barite precipitation as a result of growth on the barite surface, which has the same effect of coating the celestite substrate.

The porosities of the precipitates are in general high because the model allows precipitation in neighboring grid cells even if the grid cell itself is not completely occupied by the precipitate. While the porosity within each grid cell can approach zero in the model, the actual porosity evolves as a result of the nucleation kinetics and transport limitation in the neighboring grid cells. It is expected that additional constraint - such as only allowing precipitation in neighboring grid cells when a threshold volume fraction is reached in the 'parent' grid cell (Chen et al., 2014; Yang et al., 2021) – will result in more compact precipitates.

For the probabilistic nucleation formulations, it has been shown that the stochastic nature would be smoothed out if the spatial and temporal resolutions of the simulations are too coarse (Nooraiepour et al., 2021a). In our study, the resolutions are fine enough to maintain the relevance of the probabilistic treatment, however, we do observe sensitivity to the mesh resolution that is similar to the streamline simulations (Fig. S6). With the finer resolution, there is less barite precipitation. The range of porosity and surface coverage values remain comparable.

3.4. *Modeling limitations and prospects*

The micro-continuum model is a multi-scale approach in which a continuum domain and a pore-scale domain can be simulated simultaneously. While with certain configurations (e.g., extremely small local porosity is used in solid cells), the micro-continuum model is equivalent of a pore-scale model (Soulaine et al., 2017) and can be used to capture crystal morphology (Yang et al., 2021); it offers a unique capability of capturing sub-grid processes. This feature is especially useful in modeling precipitation systems in which nano-/micro-pores are present within the precipitates. Treating the precipitates as a continuum enables considerations of diffusive flux through the precipitates, and thus explicitly modeling of the dissolution of the primary mineral phase and the precipitation of the secondary mineral, as demonstrated in our study. The continuum formulations of subgrid properties and processes within the precipitates vary with the conceptualizations.

In most cases, description of the transport properties (e.g., diffusivity) follows the traditional continuum model approach and uses empirical relations (e.g., Archie's law), as is the case in the streamline simulations. This approach is simple, but also subject to the same challenges faced by continuum models, i.e., large uncertainties can be introduced through the empirical parameters (e.g., cementation exponent). These uncertainties can be constrained by measurements of these properties within the precipitates.

For modeling of the precipitation processes, the backbone modeling concepts of the micro-continuum model shares some similarities to those of other pore-scale models, such as the Lattice Boltzmann Model, which means that similar conceptualizations can be considered. For example, the probabilistic nucleation process has been readily implemented in our micro-continuum model and the LBM. For another example, a threshold value is typically used in LBM pore-scale models to determine whether a

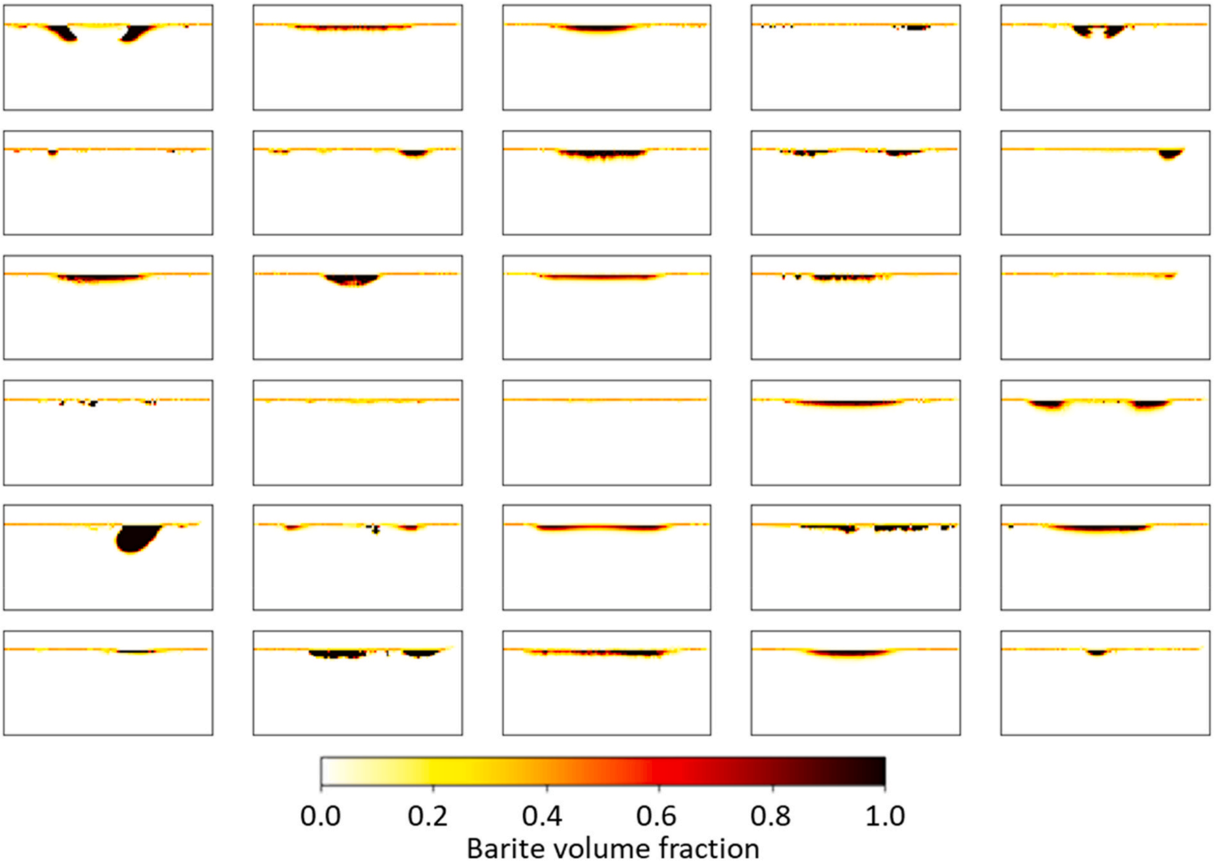

Fig. 8. Maps of the barite precipitation from 30 realizations of the probabilistic nucleation simulations with a $BaCl_2$ concentration of 100 mM and the same nucleation density on both celestite and barite. The domain is trimmed to focus on the interface.

grid becomes a solid cell and thus no further precipitation (Chen et al., 2014; Kang et al., 2010); whereas we used the minimum-porosity in our streamline simulations. In our probabilistic nucleation simulations, the remaining porosity within the precipitates is a result of local transport limitation. In the LBM model of (Varzina et al., 2020), residual porosity resulting from PCS effect was studied. It was assumed that within a grid cell, crystals of given sizes and patterns (e.g., distance between crystals) are initialized and followed by the growth of the crystals. The subgrid pore size is tracked such that pore-size controlled solubility can be calculated. As a result, the residual porosity – which is equivalent of minimum-porosity in the streamline simulations – is calculated rather than prescribed a priori. This type of conceptualization, admittedly requires more information to parameterize, can provide further mechanistic understanding.

It cannot be over-emphasized that while different conceptual models can be readily implemented in the micro-continuum model, direct observations and theoretical advances are critical for developing and testing conceptual models and their numerical implementations.

4. Conclusion

In this study, using a micro-continuum pore-scale reactive transport model, we investigated the geochemical alteration of a co-dissolution and precipitation system. The simulation results demonstrated that the dynamic development of the coating layer at the macroscopic scale is primarily controlled by the interactions between advective flow, diffusion through the coating layer, and the mineral reaction kinetics. Reactive transport modeling that considers these interactions explicitly successfully reproduced previous experimental observations of both fluid chemistry and precipitation patterns under all three saturation states. In contrast, previous continuum scale reactive transport modeling results of the same experimental system, while reproducing the fluid chemistry using empirical relations to account for the passivation effect, failed to capture some distinct features in the precipitation pattern at the lower saturation states. Furthermore, sensitivity analyses of the diffusion process across the coating layer have illustrated that the diffusion properties of the coating layer and thus the texture of the precipitates play a secondary but non-negligible role in controlling the dynamic evolution of the coating layer.

By adding a probabilistic nucleation module, we illustrated that the textures of the precipitates have a complex dependence on the saturation state and the properties of the substrate. For instance, the higher supersaturation state is more likely to result in clusters of precipitates, higher surface coverage and lower porosity in the precipitates. These exploratory simulations highlight the need of future experimental studies that provide critical mechanistic information to verify and improve conceptualizations of the modeling of ICDP processes. Our model builds on the framework of the classical nucleation theory and includes key components of current theoretical understanding of the system. Thus, the model serves as a unique tool to illustrate the dependence of precipitates' texture on fluid saturation and kinetic properties of the substrate, i.e., what would be expected based on current understanding. Because we can clearly identify the simplifications or assumptions made in the model, future studies of cross-model comparison and comparisons with direct experimental observations can help us better pinpoint areas for improvement. Such modeling effort can also help direct experimental and characterization efforts to focus on key unknowns. The framework developed here can also be adapted to incorporate more mechanistic descriptions when available, which will provide necessary information to improve treatment of the passivation effect at the continuum scale. Ultimately, it will be a combination of experimental and modeling tools that will advance our understanding of

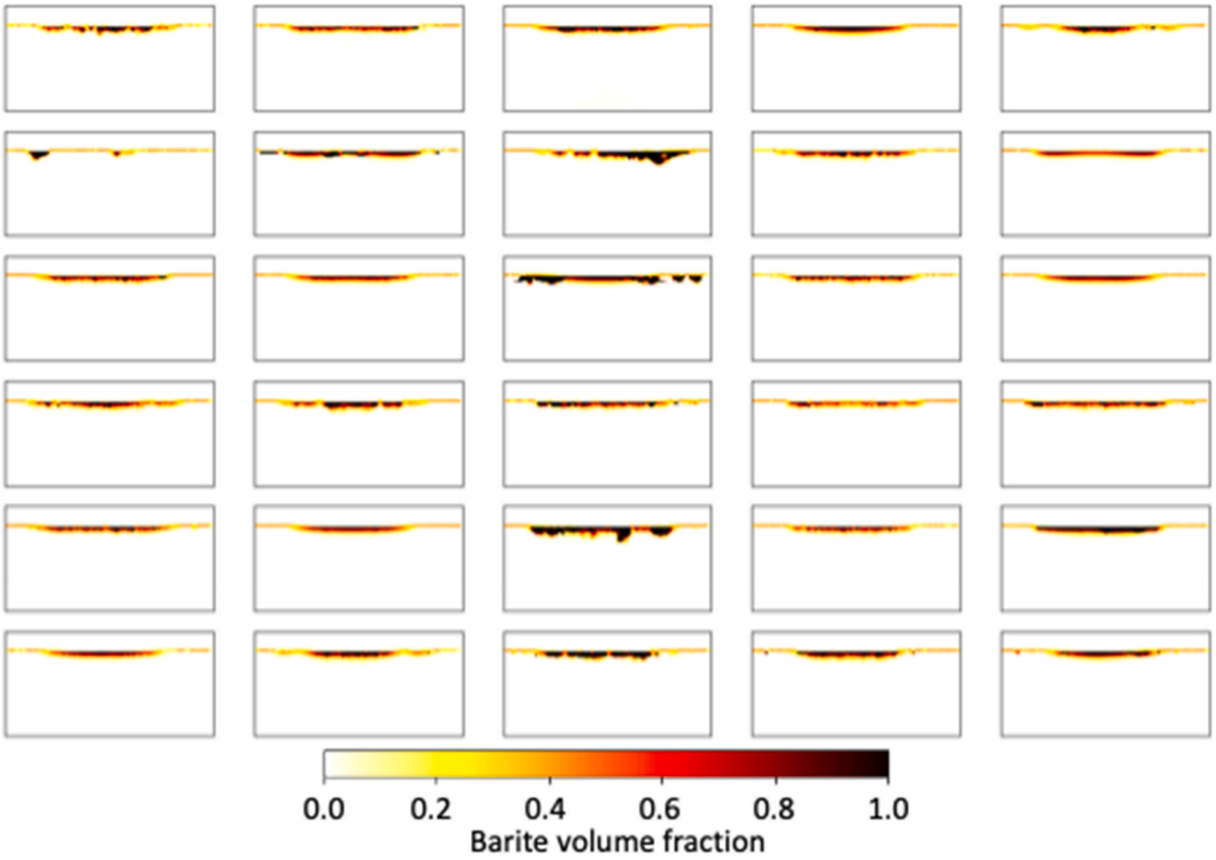

Fig. 9. Maps of the barite precipitation from 30 realizations of the probabilistic nucleation simulations with a $BaCl_2$ concentration of 100 mM and a nucleation density that is 1000 times lower on celestite than that on barite. The domain is trimmed to focus on the interface.

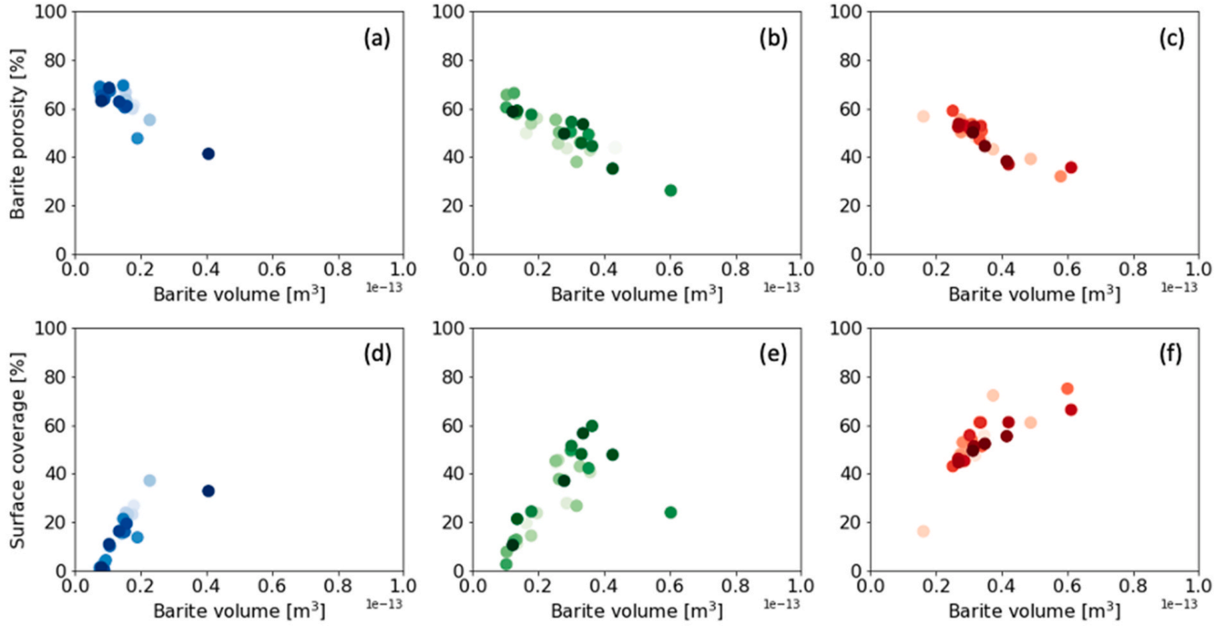

Fig. 10. (a–c) Porosity within the precipitates in relation to the barite volume, and (d–f) surface coverage in relation to the barite volume. (a,d) 10 mM $BaCl_2$, (c,e) 100 mM $BaCl_2$, and (c,f) 100 mM $BaCl_2$ with 1000x N_0. The porosity is calculated as a ratio between the total amount of barite and the total volume of grid cells with >10% occupied by barite. Barite volume is calculated assuming a thickness of 1 mm for the 2D domain. The surface coverage is calculated as the average of barite volume fraction at the interface.

ICDP processes and their impact at larger scales.

Declaration of competing interest

The authors declare that they have no known competing financial interests or personal relationships that could have appeared to influence the work reported in this paper.

Acknowledgement

The authors would like to acknowledge the funding support by the Office of Fossil Energy of the U.S. Department of Energy under Contract Number DE-AC02-05CH11231 with Lawrence Berkeley National Laboratory.

Appendix A. Supplementary data

Supplementary data to this article can be found online at https://doi.org/10.1016/j.apgeochem.2022.105207.

References

Chagneau, A., Claret, F., Enzmann, F., Kersten, M., Heck, S., Made, B., Schafer, T., 2015. Mineral precipitation-induced porosity reduction and its effect on transport parameters in diffusion-controlled porous media. Geochem. Trans. 16.

Chen, L., Kang, Q., Carey, B., Tao, W.-Q., 2014. Pore-scale study of diffusion-reaction processes involving dissolution and precipitation using the lattice Boltzmann method. Int. J. Heat Mass Tran. 75, 483–496.

Daval, D., Martinez, I., Guigner, J.M., Hellmann, R., Corvisier, J., Findling, N., Dominici, C., Goffe, B., Guyot, F., 2009. Mechanism of wollastonite carbonation deduced from micro- to nanometer length scale observations. Am. Mineral. 94, 1707–1726.

Deng, H., Molins, S., Trebotich, D., Steefel, C., DePaolo, D., 2018. Pore-scale numerical investigation of the impacts of surface roughness: upscaling of reaction rates in rough fractures. Geochem. Cosmochim. Acta 239, 374–389.

Deng, H., Navarre-Sitchler, A., Heil, E., Peters, C., 2021a. Addressing water and energy challenges with reactive transport modeling. Environ. Eng. Sci. 38, 109–114.

Deng, H., Spycher, N., 2019. Modeling reactive transport processes in fractures. Rev. Mineral. Geochem. 85, 49–74.

Deng, H., Tournassat, C., Molins, S., Claret, F., Steefel, C.I., 2021b. A pore-scale investigation of mineral precipitation driven diffusivity change at the column-scale. Water Resour. Res. 57, e2020WR028483.

Fazeli, H., Masoudi, M., Patel, R.A., Aagaard, P., Hellevang, H., 2020. Pore-scale modeling of nucleation and growth in porous media. Acs Earth Space Chem. 4, 249–260.

Forjanes, P., Astilleros, J.M., Fernández-Díaz, L., 2020. the formation of barite and celestite through the replacement of gypsum. Minerals 10.

Harrison, A.L., Dipple, G.M., Power, I.M., Mayer, K.U., 2015. Influence of surface passivation and water content on mineral reactions in unsaturated porous media: implications for brucite carbonation and CO2 sequestration. Geochem. Cosmochim. Acta 148, 477–495.

Kang, Q.J., Lichtner, P.C., Viswanathan, H.S., Abdel-Fattah, A.I., 2010. Pore scale modeling of reactive transport involved in geologic CO2 sequestration. Transport Porous Media 82, 197–213.

Kelemen, P., Benson, S.M., Pilorgé, H., Psarras, P., Wilcox, J., 2019. An overview of the status and challenges of CO2 storage in minerals and geological formations. Front. Climate. 1.

Liu, S., Jacques, D., 2017. Coupled reactive transport model study of pore size effects on solubility during cement-bicarbonate water interaction. Chem. Geol. 466, 588–599.

Luo, H.S., Quintard, M., Debenest, G., Laouafa, F., 2012. Properties of a diffuse interface model based on a porous medium theory for solid-liquid dissolution problems. Comput. Geosci. 16, 913–932.

Marty, N., Tournassat, C., Burnol, A., Giffaut, E., Gaucher, E., 2009. Influence of reaction kinetics and mesh refinement on the numerical modelling of concrete/clay interactions. J. Hydrol. 364, 58–72.

Marty, N.C.M., Claret, F., Lassin, A., Tremosa, J., Blanc, P., Made, B., Giffaut, E., Cochepin, B., Tournassat, C., 2015. A database of dissolution and precipitation rates for clay-rocks minerals. Appl. Geochem. 55, 108–118.

Mayer, K.U., Blowes, D.W., Frind, E.O., 2001. Reactive transport modeling of an in situ reactive barrier for the treatment of hexavalent chromium and trichloroethylene in groundwater. Water Resour. Res. 37, 3091–3103.

Metz, B., Davidson, O., de Coninck, H., Loos, M., Meyer, L., 2005. IPCC Special Report on Carbon Dioxide Capture and Storage. Cambridge: Cambridge University Press for the Intergovernmental Panel on Climate Change. Cambridge University Press, Cambridge, United Kingdom and New York, NY, USA.

Molins, S., Soulaine, C., Prasianakis, N.I., Abbasi, A., Poncet, P., Ladd, A.J.C., Starchenko, V., Roman, S., Trebotich, D., Tchelepi, H.A., Steefel, C.I., 2021. Simulation of mineral dissolution at the pore scale with evolving fluid-solid interfaces: review of approaches and benchmark problem set. Comput. Geosci. 25, 1285–1318.

Molins, S., Trebotich, D., Steefel, C.I., Shen, C.P., 2012. An investigation of the effect of pore scale flow on average geochemical reaction rates using direct numerical simulation. Water Resour. Res. 48, 11.

Molins, S., Trebotich, D., Yang, L., Ajo-Franklin, J.B., Ligocki, T.J., Shen, C., Steefel, C.I., 2014. Pore-scale controls on calcite dissolution rates from flow-through laboratory and numerical experiments. Environ. Sci. Technol. 48, 7453–7460.

National Academies of Sciences, Engineering, and Medicine, 2019. Negative Emissions Technologies and Reliable Sequestration: A Research Agenda. The National Academies Press, Washington, DC. https://doi.org/10.17226/25259.

Noiriel, C., Soulaine, C., 2021. Pore-Scale Imaging and Modelling of Reactive Flow in Evolving Porous Media: Tracking the Dynamics of the Fluid–Rock Interface. Transport in Porous Media 140, 181–213.

Noiriel, C., Steefel, C.I., Yang, L., Ajo-Franklin, J., 2012. Upscaling calcium carbonate precipitation rates from pore to continuum scale. Chem. Geol. 318, 60–74.

Nooraiepour, M., Masoudi, M., Hellevang, H., 2021a. Probabilistic nucleation governs time, amount, and location of mineral precipitation and geometry evolution in the porous medium. Sci. Rep. 11.

Nooraiepour, M., Masoudi, M., Shokri, N., Hellevang, H., 2021b. Probabilistic nucleation and crystal growth in porous medium: new insights from calcium carbonate precipitation on primary and secondary substrates. ACS Omega 6, 28072–28083.

Palandri, J.L., 2004. A Compilation of Rate Parameters of Water-Mineral Interaction Kinetics for Application to Geochemical Modeling [electronic Resource]/by James L. Palandri and Yousif K. Kharaka ; Prepared in Cooperation with the National Energy Technology Laboratory. United States Department of Energy. U.S. Dept. of the Interior, U.S. Geological Survey, Menlo Park, Calif.

Perko, J., Ukrainczyk, N., Savija, B., Phung, Q.T., Koenders, E.A.B., 2020. Influence of micro-pore connectivity and micro-fractures on calcium leaching of cement pastes-A coupled simulation approach. Materials 13.

Poonoosamy, J., Curti, E., Kosakowski, G., Grolimund, D., Van Loon, L.R., Mäder, U., 2016. Barite precipitation following celestite dissolution in a porous medium: a SEM/BSE and μ-XRD/XRF study. Geochem. Cosmochim. Acta 182, 131–144.

Poonoosamy, J., Haber-Pohlmeier, S., Deng, H., Deissmann, G., Klinkenberg, M., Gizatullin, B., Stapf, S., Brandt, F., Bosbach, D., Pohlmeier, A., 2020a. Combination of MRI and SEM to assess changes in the chemical properties and permeability of porous media due to barite precipitation. Minerals 10.

Poonoosamy, J., Klinkenberg, M., Deissmann, G., Brandt, F., Bosbach, D., Mäder, U., Kosakowski, G., 2020b. Effects of solution supersaturation on barite precipitation in porous media and consequences on permeability: experiments and modelling. Geochem. Cosmochim. Acta 270, 43–60.

Poonoosamy, J., Soulaine, C., Burmeister, A., Deissmann, G., Bosbach, D., Roman, S., 2020c. Microfluidic flow-through reactor and 3D Raman imaging for in situ assessment of mineral reactivity in porous and fractured porous media. Lab Chip 20, 2562–2571.

Poonoosamy, J., Westerwalbesloh, C., Deissmann, G., Mahrous, M., Curti, E., Churakov, S.V., Klinkenberg, M., Kohlheyer, D., von Lieres, E., Bosbach, D., Prasianakis, N.I., 2019. A microfluidic experiment and pore scale modelling diagnostics for assessing mineral precipitation and dissolution in confined spaces. Chem. Geol. 528.

Prasianakis, N.I., Curti, E., Kosakowski, G., Poonoosamy, J., Churakov, S.V., 2017. Deciphering pore-level precipitation mechanisms. Sci. Rep. 7.

Prieto, M., 2014. Nucleation and supersaturation in porous media (revisited). Mineral. Mag. 78, 1437–1447.

Qiu, Q., 2020. A state-of-the-art review on the carbonation process in cementitious materials: fundamentals and characterization techniques. Construct. Build. Mater. 247, 118503.

Rajyaguru, A., L'Hopital, E., Savoye, S., Wittebroodt, C., Bildstein, O., Arnoux, P., Detilleux, V., Fatnassi, I., Gouze, P., Lagneau, V., 2019. Experimental characterization of coupled diffusion reaction mechanisms in low permeability chalk. Chem. Geol. 503, 29–39.

Renard, F., Røyne, A., Putnis, C.V., 2019. Timescales of interface-coupled dissolution-precipitation reactions on carbonates. Geosci. Front. 10, 17–27.

Ruiz-Agudo, C., Putnis, C.V., Ruiz-Agudo, E., Putnis, A., 2015. The influence of pH on barite nucleation and growth. Chem. Geol. 391, 7–18.

Seigneur, N., Mayer, K.U., Steefel, C.I., 2019. Reactive transport in evolving porous media. Rev. Mineral. Geochem. 85, 197–238.

Soulaine, C., Maes, J., Roman, S., 2021. Computational microfluidics for geosciences. Front. Water 3.

Soulaine, C., Roman, S., Kovscek, A., Tchelepi, H.A., 2017. Mineral dissolution and wormholing from a pore-scale perspective. J. Fluid Mech. 827, 457–483.

Varzina, A., Cizer, Ö., Yu, L., Liu, S., Jacques, D., Perko, J., 2020. A new concept for pore-scale precipitation-dissolution modelling in a lattice Boltzmann framework – application to portlandite carbonation. Appl. Geochem. 123, 104786.

Xiong, W., Deng, H., Moore, J., Crandall, D., Hakala, J.A., Lopano, C., 2021. Influence of Flow Pathway Geometry on Barite Scale Deposition in Marcellus Shale during Hydraulic Fracturing. Energy & Fuels.

Yang, F., Stack, A.G., Starchenko, V., 2021. Micro-continuum approach for mineral precipitation. Sci. Rep. 11, 3495.

Yoon, H., Valocchi, A.J., Werth, C.J., Dewers, T., 2012. Pore-scale simulation of mixing-induced calcium carbonate precipitation and dissolution in a microfluidic pore network. Water Resour. Res. 48 (n/a).

Zhang, C.Y., Dehoff, K., Hess, N., Oostrom, M., Wietsma, T.W., Valocchi, A.J., Fouke, B. W., Werth, C.J., 2010. Pore-scale study of transverse mixing induced CaCO3 precipitation and permeability reduction in a model subsurface sedimentary system. Environ. Sci. Technol. 44, 7833–7838.

Zhang, Q., Deng, H., Dong, Y., Molins, S., Li, X., Steefel, C.I., 2022. Investigation of coupled processes in fractures and the bordering matrix via a micro-continuum reactive transport model. Water Res. Res. Accep. https://doi.org/10.1029/2021WR030578.